

Tortuosity Anisotropy in Lithium-Ion Battery Electrodes

Martin Ebner, Ding-Wen Chung, R. Edwin García, and Vanessa Wood*

High-performance lithium-ion batteries (LIBs) require improved active materials and optimized porous electrode microstructures. Both experimental and computational studies have demonstrated that the microstructure of LIB electrodes influences key performance metrics.^[1–7] For example, the experimental study of graphite by Buqa et al. in 2005 reported the dependence of rate-performance on controllable electrode fabrication parameters such as porosity and loading and suggests that the obtained performance is linked to the tortuous electrode microstructure formed by graphite platelets.^[3] More recently, inhomogeneous lithiation and metallic lithium plating on spherical mesocarbon microbead (MCMC) electrodes has been imaged in situ by Harris et al.^[7] Subsequently, these effects, which limit durability and safety of LIBs, were linked to microstructural inhomogeneity.^[8]

The reason why microstructure has an impact on LIB performance metrics such as charge and discharge rate, cell life, and safety is conceptually clear.^[8] In industrial LIB electrode manufacturing, a suspension of active particles, conductive agents, and polymeric binder in a solvent is cast and dried, and calendaring is used to achieve the dense, low porosity electrodes required for high energy density batteries.^[9] This manufacturing process does not allow for microstructure control, such that complex, tortuous microstructures can result, leading to decreased effective electrolyte conductivity and diffusivity. Because transport in the electrolyte phase limits performance for materials such as graphite with fast solid-state diffusivities of interest for high rate capability, the microstructure of the porous electrodes becomes critical.^[2] In this work, we seek to quantify parameters that control porous electrode manufacturing, such as particle shape and calendaring, and its impact on microstructural properties that are key to controlling battery performance and reliability.

In the macroscopic description of porous electrodes, the concept of electrode tortuosity (τ) is used along with electrode porosity (ϵ) as a measure for the decrease in effective electrolyte conductivity and diffusivity due to the microstructure of the electrode. To highlight the impact that tortuosity and porosity can have on electrode performance, we simulate the discharge behavior of a high energy graphite electrode with a loading of 10 mAh cm⁻². For a specific material set where the

porosity can be systematically varied, tortuosity and porosity are related quantities. This is expressed through the generalized Bruggeman relation^[10]

$$\tau = \epsilon^{-\alpha} \quad (1)$$

Figure 1a shows the maximum rate delivering 80% of the nominal discharge capacity as a function of electrode porosity. Each curve corresponds to different tortuosity–porosity relations, parameterized by different values of α , ranging from 0.5 to 4. As expected, low porosity electrodes of about 30%, which are desirable due to their high energy density, show a maximum rate of 1/2 C, i.e., nominal discharge in 2 h, for a Bruggeman exponent $\alpha = 2$, whereas $\alpha = 0.5$ would allow for 2 C discharges, i.e., nominal discharge in 1/2 h. Details of the simulations and results for other electrode loadings are available in the Supporting Information (Figure S2). The importance of low tortuosity is further highlighted by recent results demonstrating the electrodes fabricated with novel techniques to minimize tortuosity in the direction perpendicular to the current collector can enhance fast lithium transport deep into the electrode.^[11–13] While these manufacturing techniques remain far from commercialization, the high economic relevance of fast charge- and dischargeable batteries speaks to the need to quantify and understand direction-specific tortuosity (i.e., tortuosity anisotropy). While some studies provide a few directional tortuosity values, no extensive study of tortuosity anisotropy and its relation to particle shape and processing conditions exists.^[14–17]

As outlined in Figure 1b, here we experimentally and theoretically quantify and determine the origin of tortuosity anisotropy in porous electrodes. We fabricate electrodes with a range of porosities from different active materials and acquire 3D representations of the electrodes microstructures using synchrotron radiation X-ray tomographic microscopy (SRXTM). We perform numerical diffusion simulations on the obtained microstructure representations to determine in-plane (i.e., parallel to the current collector) and through-plane (i.e., perpendicular to the current collector) tortuosities.^[18] Then, we investigate the validity of the differential effective medium (DEM) approximation for calculating tortuosity in porous electrodes by using the distribution of particle sizes, shapes, and orientation, obtained by identifying individual particles in the 3D microstructure datasets.^[19] Finally, we test if particle size and shape information extracted from a relatively small number of particles in scanning electron microscopy (SEM) images, a technique readily available to most researchers, is sufficient input to yield accurate directional tortuosity values from the DEM approximation.

Tortuosity has traditionally been difficult to quantify, and disparate values in the range of 1–12 for electrode porosities of 20–70% have been found.^[14–17] Furthermore, electrochemical methods permit measurement of through-plane tortuosity, but not in-plane tortuosity, rendering quantification of tortuosity

M. Ebner, Prof. V. Wood
Department of Information Technology
and Electrical Engineering
ETH Zurich, 8092, Zurich, Switzerland
E-mail: vwood@ethz.ch
D.-W. Chung, Prof. R. E. García
School of Materials Engineering
Purdue University
West Lafayette, IN, 47907, USA.



DOI: 10.1002/aenm.201301278

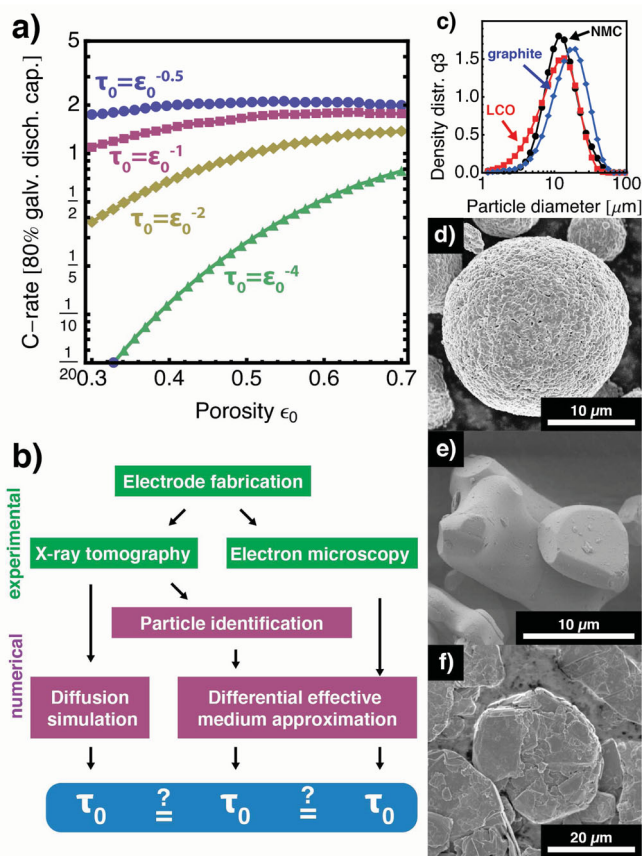


Figure 1. a) Maximum discharge rates yielding 80% of nominal capacity as a function of electrode porosity for different Bruggeman exponents α . b) Outline of manuscript content. c) Particle size distributions of LCO, NMC, and graphite powders obtained by laser diffraction demonstrate the comparable particle sizes and size distributions. Scanning electron microscopy images of d) spherical NMC, e) non-spherical LCO, and f) platelet-shaped graphite particles.

anisotropy impossible.^[14] We recently demonstrated that diffusion simulations performed on large volume, 3D microstructure reconstructions of real battery electrodes imaged with SRXTM enable quantification of tortuosity and investigation of the effect of electrode inhomogeneity on tortuosity.^[20] Here, we use this technique to probe tortuosity anisotropies that originate from active material selection and the manufacturing process.^[21]

We design an experiment to determine the anisotropic tortuosity of electrodes fabricated from particles, which span a range of shapes relevant for battery applications, including spheres (principal axes $a = b = c$), triaxial ellipsoids ($a > b > c$), and platelets ($a > b \gg c$). As model material systems, we selected spherical $\text{LiNi}_{1/3}\text{Mn}_{1/3}\text{Co}_{1/3}\text{O}_2$ (NMC), triaxial LiCoO_2 (LCO), and platelet-shaped graphite because these materials are commercially available with comparable particle size distributions (PSD), facilitating study of the effect of particle shape on tortuosity, independent of particle size or size-distribution. PSD, determined by laser diffraction, and SEM images of all material sets are depicted in Figure 1. The choice of LCO and NMC is primarily based on particle

shape and compatibility to X-ray tomography, not to showcase microstructure induced ionic transport limitations, which for these materials only govern battery performance for thick and dense electrodes at high C-rates.^[22,23] However, as discussed previously, graphite electrodes, due to the high electronic conductivity and reasonably fast solid-state diffusion of lithium in graphite, are prone to microstructure induced ionic transport limitations.^[2,3,24] We emphasize that our findings in this work are based on purely geometrical arguments and make no assumption about the electrochemical performance of a material. They are therefore applicable to any electrochemical material set.

The collected tomography data allow us to extract the active phase porosity and, using numerical diffusion simulations, directional tortuosity. Directional tortuosity of 39 electrodes fabricated with different porosities from NMC, LCO, and graphite are summarized in Figure 2a–c. The exponent α of Equation 1 was fit to the obtained data for each principal direction.^[10,25] Electrodes featuring spherical NMC particles do not show significant tortuosity anisotropy (i.e., tortuosity values from three orthogonal directions of each electrode lie in close proximity). In addition, the directional Bruggeman exponent for spherical NMC particles (Table 1) is close to the value $\alpha = 0.5$, which is expected for porous structures of spherical particles. In contrast, non-spherical LCO particles give rise to anisotropic tortuosity. Tortuosity values of the two in-plane directions as a function of porosity are comparable in magnitude, but the corresponding through-plane tortuosity is significantly higher, especially at low porosities. The tortuosity anisotropy of the graphite system is even more pronounced with a Bruggeman exponent $\alpha = 1.9$ for the through-plane direction. For example, the through-plane tortuosity of electrodes with a porosity of 40% is three times the value of the in-plane tortuosities. Such an increase in through-plane tortuosity and the resulting decrease in the macroscopic diffusion coefficient and conductivity in the pore-filling electrolyte have considerable implications for the lithium transport, as showcased in Figure 1a.^[1–3]

To understand the relation between the tortuosity anisotropy in the electrode and the particle shape anisotropy, we apply the particle identification algorithm developed in ref. [21] to binarized microstructures of NMC and LCO electrodes, examples of which are shown as insets in Figure 2a,b. The shape and orientation of all individual NMC and LCO particles in the electrodes is quantified by fitting general ellipsoids to each identified particle and by studying the ratios between the ellipsoid principal axes as well as the angle each principal axis makes with respect to the plane of the current collector (i.e., the elevation angle).^[26] Figure 2d,e provide the distribution of NMC and LCO particle shapes, according to a shape classification scheme introduced by Zingg.^[27] In this representation, a perfect sphere ($a = b = c$) is located in the lower right corner of the diagram, a perfect disc ($a = b, c = 0$) in the lower left and a perfect needle ($b = c = 0$) in the upper left corner. Coloring in the diagram indicates the shape exhibited by particles in the measured electrodes with dark colors corresponding to large volume fractions. It is apparent that the NMC particles are indeed spherical in nature as their distribution lies within the equant region of the diagram near the spherical extreme. In contrast, the LCO particles have a broad shape distribution with a maximum near the

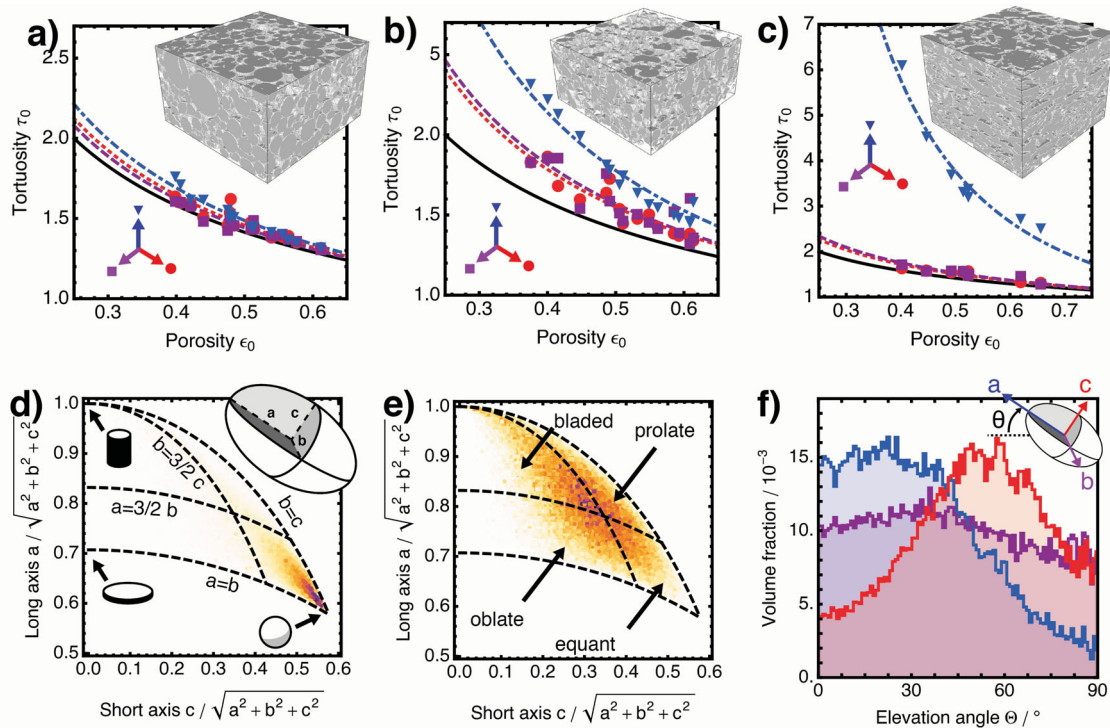


Figure 2. Tortuosity-porosity relations obtained by numerical diffusion simulations carried out on synchrotron X-ray tomography data for a) NMC, b) LCO, and c) graphite electrodes with insets showing microstructure renderings of typical electrodes. Note different axes scaling. Particle shape distributions reveal and quantify the d) spherical particle shape of NMC and e) non-spherical shape of LCO. The dotted lines indicate the geometric limits and differentiate between regions of distinct particle shapes. f) Orientation statistics of the long (blue), median (purple), and short principal axes (red) of non-spherical LCO particles within the porous electrode. Particles preferentially align their long principal axis a horizontally, as seen by the high volume fraction near elevation angle 0° .

crossover point of all regions, demonstrating that they do not exhibit preferential spherical, disc, or needle shape.

Figure 2f depicts the distribution of principal axes orientations for LCO determined from the tomography data. The non-spherical LCO particles exhibit distinct alignment of their longest principal axes parallel to the plane of the current collector (i.e., small elevation angle). The shortest principal axes are oriented perpendicular to the current collector with a large elevation angle. Spherical NMC particles show some alignment

(Figure S4 in the Supporting Information), but because the principal axes are all similar in length (i.e., $a \approx b \approx c$), this does not lead to a significant tortuosity anisotropy. These results highlight that alignment of non-spherical particles with their longest principal axes parallel to the current collector is the cause of tortuosity anisotropy.

To understand the relative importance of 1) gravity during slurry coating and subsequent drying and 2) calendaring of the dry electrode on causing the observed particle alignment, we compare orientation statistics of compressed and uncompressed electrodes. Figure S5 (Supporting Information) provides alignment statistics for all 16 LCO electrodes. We find that uncompressed electrodes already feature aligned particles indicating that gravity plays a role. Increasing calendaring pressure leads to only a small additional increase in alignment for all electrodes. Statistics of individual NMC electrodes (Figure S4, Supporting Information) show weak trends in particle alignment, except for highly compressed electrodes that exhibit surprisingly distinct alignment. We conjecture that fragments of fractured particles, as observed in these electrodes (discussed in ref. [21]), align.

We assess whether our findings that electrodes composed of non-spherical particles exhibit pronounced anisotropic tortuosity and that in-plane, horizontal, particle alignment during electrode manufacturing is responsible for the observed

Table 1. Bruggeman exponent α , determined by least-square fitting Equation 1 to the porosity-tortuosity data shown in Figure 2 and 3.

	X (in-plane)	Y (in-plane)	Z (through-plane)
NMC	0.544	0.528	0.573
NMC + inactive	0.531	0.520	0.558
NMC DEM	0.539	0.551	0.590
LCO	0.632	0.651	0.830
LCO + inactive	0.597	0.613	0.754
LCO DEM	0.656	0.664	0.843
Graphite	0.591	0.614	1.914
Graphite DEM	0.666	0.666	1.949

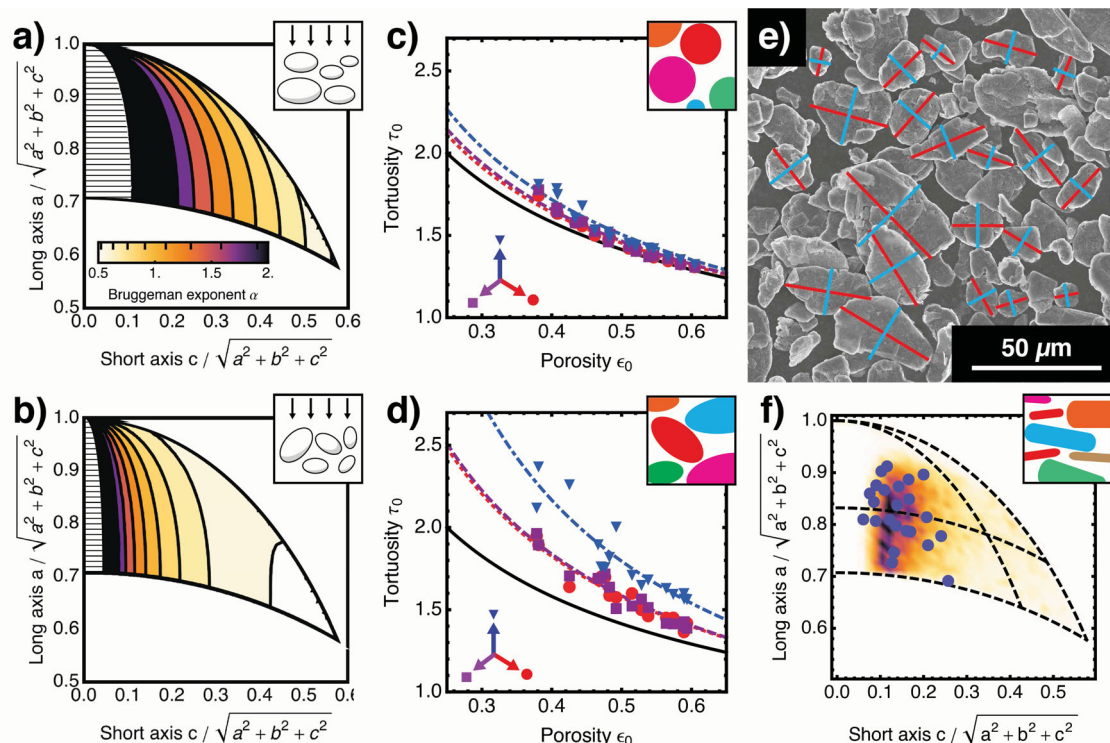


Figure 3. Bruggeman exponent α estimated by the DEM approximation as a function of ellipsoid shape for a) perfectly aligned ellipsoids in the direction of the shortest principal axis and b) for randomly oriented ellipsoids. Knowledge of individual particle shape, size, and orientation for c) NMC and d) LCO allows estimation of tortuosity for specific porosities by the DEM approximation. The data points represent the tortuosities estimated by DEM, the dashed lines show best fits to Equation 1. These data points and the fitted Bruggeman exponents are in good agreement with those calculated from numerical diffusion simulations on the X-ray tomography data sets. e) SEM image of graphite powder with color bars indicating measures of principal axes a and b for individual particles. f) Particle shape diagram with individual points obtained through analysis of the SEM image in (e). The shaded area indicates the simulated particle shape distribution used for the DEM prediction.

tortuosity anisotropy can be understood in the context of the DEM approximation. The DEM approximation (see Supporting Information) was introduced by Bruggeman, and is generalized through Equation 1.^[10,19] In the context of battery research, the exponent, α , has often simply been chosen to be $\alpha = 0.5$.^[28] However, $\alpha = 0.5$ is valid only in the case of spherical, monodispersed particles.^[20] For non-spherical particles, the Bruggeman exponent can also be calculated in the context of the DEM approximation based on experimental or assumed knowledge of particle shape and orientation.^[19] **Figure 3a,b** show the Bruggeman exponent calculated with the DEM approximation for all particle shapes in two extreme cases: for particles that 1) have their shortest principal axis aligned to the direction of tortuosity estimation and 2) for particles that are randomly oriented. For aligned particles (**Figure 3a**), the expected Bruggeman exponent increases quickly for increasing particle aspect ratio. In contrast, in the case of randomly oriented particles (**Figure 3b**), the Bruggeman exponent increases more moderately. This highlights the dependency of tortuosity anisotropy on the interplay between particle shape and alignment. Finally, as shown in **Figure S6** (Supporting Information), if particles have their longest principal axis aligned to the direction of transport, the Bruggeman exponent can be reduced below 0.5. In such a case, the data shown in **Figure 2c** highlight that a reduction in through-plane tortuosity by a factor of about 3 over

current graphite electrodes could be achieved. These results provide a clear design guideline: if particle alignment cannot be controlled during electrode manufacturing, spherical particles are desirable; however, if advanced manufacturing tools are available that enable controlled particle alignment, tortuosity can be decreased far below what is accessible through the use of spherical particles.

The detailed NMC and LCO particle shape and alignment information obtained through tomography and subsequent particle identification allows us to apply a discrete version of the DEM approximation to determine electrode tortuosity and compare the results to tortuosity values predicted through numerical diffusion simulations performed directly on the X-ray tomography data. **Figure 3c,d** plot the anisotropic tortuosities obtained through the DEM approximation. Values for directional Bruggeman exponents α determined by fitting Equation 1 to the data points calculated with the DEM approximation are in excellent agreement with the values obtained through numerical diffusion simulations on the X-ray tomography data, as shown in **Table 1**.

Because the DEM approximation successfully accounts for the experimentally observed tortuosity anisotropy for spherical NMC and non-spherical LCO electrode microstructures, we next assess whether the DEM approximation can be also used as a predictive tool. Here, we extract the shape of 23 particles

from the SEM image of the graphite particles shown in Figure 3e, mark them in the shape diagram of Figure 3f, and estimate the moments of the underlying shape distribution (normal distributed, $\mu_{a/b} = 1$, $\sigma_{a/b} = 0.8$, $a > b$, $\mu_{a/c} = 5$, $\sigma_{a/c} = 2$, $a > c$). To model this distribution, a set of particles is randomly drawn from a computer-generated population. The resulting shape distribution is overlaid as the shaded area in Figure 3f. In addition, a normal distribution of elevation angles ($\mu_\theta = 0^\circ$, $\sigma_\theta = 25^\circ$) is assumed and a log-normal volume distribution that matches the measured graphite PSD shown in Figure 1c is chosen. Using this shape, alignment, and volume information and applying the DEM approximation, the in-plane and through-plane Bruggeman exponents are estimated to be 0.66 and 1.94, respectively. These Bruggeman exponents are in agreement with those calculated through the numerical diffusion simulations performed directly on the tomography data (Table 1). This procedure demonstrates that simple visual characterization of particle morphology, in combination with the DEM approximation, enables rapid assessment of the tortuosity tensor for arbitrary particle shapes.

In conclusion, using X-ray tomography data collected from 39 porous electrodes, we demonstrate that non-spherical active material particles translate their anisotropic shape into an anisotropic electrode microstructure due to alignment of the particles parallel to the current collector during electrode manufacturing. The increased tortuosity in the plane perpendicular to current collection can impact the achievable power density and cycling performance of a LIB, clearly motivating the use of spherical active material particles if only standard porous electrode manufacturing techniques are available. Our results demonstrate that by utilizing spherical graphite particles or aligning platelet-shaped particles, a factor of 4 improvement in discharge rate can be obtained.

Furthermore, by comparing the tortuosity values for the experimentally determined electrode microstructures from numerical diffusion simulation, we demonstrate that the DEM approximation provides an excellent estimate for tortuosity, which can thus be used in the development of advanced porous electrochemical simulations or to select electrode thickness and porosity for a desired LIB performance. The use of a simple visual analysis to estimate particle shape through SEM coupled with knowledge of the particle size distribution and estimation of particle alignment, the DEM approximation provides a practical method to assess the average directional tortuosity without the need of complex electrochemical techniques or infrastructure intensive tomography measurements and simulations. Indeed, the Bruggeman exponent maps provided in Figure 3a,b enable a priori assessment of the impact of a specific active material morphology on in-plane and through-plane porous electrode tortuosity, thereby facilitating rational design of high performance battery electrodes.

Experimental Section

Materials: Spherical $\text{LiNi}_{1/3}\text{Mn}_{1/3}\text{Co}_{1/3}\text{O}_2$ (NMC) was received from 3M Co., St. Paul, Minnesota, USA, non-spherical LiCoO_2 (LCO) from Umicore, Brussels, Belgium, graphite and carbon black (Super C65) from TIMCAL Ltd., Bodio, Switzerland, and Kynar 761 binder from Arkema, Philadelphia, PA, USA. Other materials were purchased:

N-methyl pyrrolidone solvent (NMP, biotech grade) from Sigma-Aldrich Chemie GmbH, Buchs, Switzerland and LP30 electrolyte, containing 1 M LiPF₆ in a 1:1 mass-ratio mixture of ethylene carbonate (EC) and dimethyl carbonate (DMC) from Merck, Germany.

Preparation of Electrodes: Electrode slurries with weight ratios of active material to carbon black to binder of 96:2:2, 94:3:3, 92:4:4, and 90:5:5 in NMP solvent were prepared. The ingredients were mixed for 5 min using a high-shear disperser, rested on a roller bench for up to 3 h to remove bubbles, and cast onto 12 μm thick aluminum or copper foils with an automatic film applicator using a notch bar. The films were then dried under vacuum for 8 h at 80 $^\circ\text{C}$ and electrodes with a diameter of 13 mm were punched out with a proprietary puncher.

Compression of Electrodes: Electrodes were compressed at room temperature during 6 cycles with increasing pressure in a proprietary calendaring machine with 80 mm roll diameter. The roller applied a load per unit length of 36.3, 72.5 and 241.6 N mm^{-1} on the electrodes, resulting in pressures of approximately 300, 600, and 2000 bar. The electrodes comprising the spherical NMC particles are the same as those described in ref. [21].

Tomography Experiments and Numerical Analysis: Porous electrode preparation for SRXTM, experimental details of SRXTM, 3D reconstruction, and data segmentation to identify individual particles followed the approach described in ref. [21]. The orientation and shape of individual particles was estimated by fitting a general ellipsoid to each particle identified from the tomography data using a MATLAB script.^[26] These fits were used to quantify particle shape distributions and particle alignment. Tortuosity calculation followed the method developed by Vijayaraghavan et al.^[18] on cuboid subsections of the obtained microstructures. In short, the steady state mass flux density was calculated by discretization of the diffusion equation in the pore-space of the binarized microstructure, while the surface of the solid phase was treated as an insulating boundary. Two fixed virtual concentrations were enforced on two opposing surfaces of the cuboid microstructure subsections while the other four surfaces were treated as insulating boundaries. From the obtained steady state mass flux density, tortuosity in the direction of the mass flux was calculated.

Differential Effective Medium Approximation: For non-spherical particles such as ellipsoids, α can be calculated according to ref. [19]. The exponent $\alpha_i = R_i$ in i -direction for perfectly aligned, identical ellipsoidal particles with principal axes α_i in d dimensions can be calculated using Equation (2) and (3), from which the exponent $\alpha_{\text{random}} = R_{\text{random}}$ for randomly aligned particles can be derived using Equation (4).

$$A_i^* = \frac{1}{2} \prod_{j=1}^d a_j \int_0^\infty \frac{dt}{(t + \alpha_j^2) \sqrt{\prod_{j=1}^d (t + \alpha_j^2)}} \quad (2)$$

$$R_i = \frac{1}{1 - A_i^*} \quad i = 1, \dots, d \quad (3)$$

$$R_{\text{random}} = \frac{1}{d} \sum_{i=1}^d R_i \quad (4)$$

Supporting Information

Supporting Information is available from the Wiley Online Library or from the author.

Acknowledgements

The authors gratefully acknowledge material donations from 3M, Umicore, TIMCAL, and Arkema. They thank Prof. Andreas Mortensen for the fruitful discussion of differential effective medium theory, Dr. Marone and Prof. Stampanoni for support with the tomography setup,

Prof. Petr Novak for use of the proprietary compression roller and design of electrochemical cells, Prof. David Norris for use of the SEM, and Prof. Philipp Rudolf von Rohr for use of the particle size analyzer. The tomography experiments were performed on the TOMCAT beamline at the Swiss Light Source, Paul Scherrer Institut, Villigen, Switzerland. M.E. and V.W. acknowledge funding of this project by the Gebert R f Stiftung under project number GRS-009/13 and the Commission for Technology and Innovation in Switzerland. D.W.C. and R.E.G. are grateful for the support provided by National Science Foundation CMMI 0856491.

Received: August 23, 2013

Published online:

- [1] S. Elul, Y. Cohen, D. Aurbach, *J. Electroanal. Chem.* **2012**, 682, 53.
- [2] M. He , P. Nov k, *Electrochim. Acta* **2013**, 106, 149.
- [3] H. Buqa, D. Goers, M. Holzapfel, M. E. Spahr, P. Nov k, *J. Electrochem. Soc.* **2005**, 152, A474.
- [4] Y.-H. Chen, C.-W. Wang, X. Zhang, A. M. Sastry, *J. Power Sources* **2010**, 195, 2851.
- [5] P. Arora, M. Doyle, A. S. Gozdz, R. E. White, J. Newman, *J. Power Sources* **2000**, 88, 219.
- [6] S. J. Dillon, K. Sun, *Curr. Opin. Solid St. Mater. Sci.* **2012**, 16, 153.
- [7] S. J. Harris, A. Timmons, D. R. Baker, C. Monroe, *Chem. Phys. Lett.* **2010**, 485, 265.
- [8] S. J. Harris, P. Lu, *J. Phys. Chem. C* **2013**, 117, 6481.
- [9] T. Marks, S. Trussler, A. J. Smith, D. Xiong, J. R. Dahn, *J. Electrochem. Soc.* **2011**, 158, A51.
- [10] D. A. Bruggeman, *Ann. Phys.* **1935**, 416, 636.
- [11] J. W. Long, B. Dunn, D. R. Rolison, H. S. White, *Chem. Rev.* **2004**, 104, 4463.
- [12] C.-J. Bae, C. K. Erdonmez, J. W. Halloran, Y.-M. Chiang, *Adv. Mater.* **2013**, 25, 1254.
- [13] H. Zhang, X. Yu, P. V. Braun, *Nat. Nanotechnol.* **2011**, 6, 277.
- [14] I. V. Thorat, D. E. Stephenson, N. A. Zacharias, K. Zaghib, J. N. Harb, D. R. Wheeler, *J. Power Sources* **2009**, 188, 592.
- [15] N. A. Zacharias, D. R. Nevers, C. Skelton, K. Knackstedt, D. E. Stephenson, D. R. Wheeler, *J. Electrochem. Soc.* **2013**, 160, A306.
- [16] D. Kehrwald, P. R. Shearing, N. P. Brandon, P. K. Sinha, S. J. Harris, *J. Electrochem. Soc.* **2011**, 158, A1393.
- [17] T. Hutzenlaub, A. Asthana, J. Becker, D. R. Wheeler, R. Zengerle, S. Thiele, *Electrochem. Commun.* **2013**, 27, 77.
- [18] B. Vijayaraghavan, D. R. Ely, Y.-M. Chiang, R. Garc a-Garc a, R. E. Garc a, *J. Electrochem. Soc.* **2012**, 159, A548.
- [19] S. Torquato, *Random Heterogeneous Materials*, Springer, New York **2002**.
- [20] D.-W. Chung, M. Ebner, D. R. Ely, V. Wood, R. E. Garc a, *Model. Simul. Mater. Sci. Eng.* **2013**, 21, 074009.
- [21] M. Ebner, F. Geldmacher, F. Marone, M. Stampanoni, V. Wood, *Adv. Energy Mater.* **2013**, 3, 845.
- [22] H. Zheng, J. Li, X. Song, G. Liu, V. S. Battaglia, *Electrochim. Acta* **2012**, 71, 258.
- [23] H. Zheng, L. Tan, G. Liu, X. Song, V. S. Battaglia, *J. Power Sources* **2012**, 208, 52.
- [24] K. Persson, V. A. Sethuraman, L. J. Hardwick, Y. Hinuma, Y. S. Meng, A. van der Ven, V. Srinivasan, R. Kostecki, G. Ceder, *J. Phys. Chem. Lett.* **2010**, 1, 1176.
- [25] J. Newman, K. E. Thomas-Alyea, *Electrochemical Systems*, Wiley, Hoboken, NJ **2004**.
- [26] Y. Petrov, Ellipsoid fit, <http://www.mathworks.com/matlabcentral/fileexchange/24693-ellipsoid-fit>, (accessed May 2013).
- [27] T. Zingg, *Schweiz. Mineral. Petrogr. Mitt.* **1935**, 15, 39.
- [28] M. Doyle, T. F. Fuller, J. Newman, *J. Electrochem. Soc.* **1993**, 140, 1526.